

Reductive Transformations of a Pyrazolate-Based Bioinspired Diiron–Dinitrosyl Complex

Nicole Kindermann,[†] Anne Schober,[†] Serhiy Demeshko,[†] Nicolai Lehnert,[‡] and Franc Meyer^{*,†}

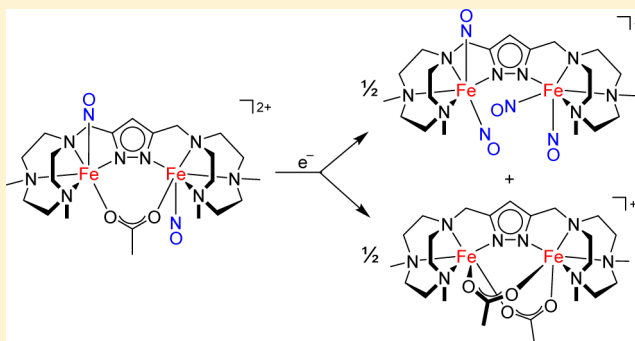
[†]Institut für Anorganische Chemie, Georg-August-Universität Göttingen, Tammannstraße 4, 37077 Göttingen, Germany

[‡]Department of Chemistry, The University of Michigan, 930 N. University Avenue, Ann Arbor, Michigan 48109-1055, United States

S Supporting Information

ABSTRACT: Flavo-diiron nitric oxide reductases (FNORs) are a subclass of nonheme diiron proteins in pathogenic bacteria that reductively transform NO to N₂O, thereby abrogating the nitrosative stress exerted by macrophages as part of the immune response. Understanding the mechanism and intermediates in the NO detoxification process might be crucial for the development of a more efficient treatment against these bacteria. However, low molecular weight models are still rare, and only in a few cases have their reductive transformations been thoroughly investigated. Here, we report on the development of two complexes, based on a new dinucleating pyrazolate/triazacyclononane hybrid ligand L[−], which serve as model systems for nonheme diiron active sites.

Their *ferrous* nitrile precursors [L{Fe(R'CN)}₂(μ-OOCR)](X)₂ (**1**) can be readily converted into the corresponding nitrosyl adducts ([L{Fe(NO)}₂(μ-OOCR)](X)₂, **2**). Spectroscopic characterization shows close resemblance to nitrosylated nonheme diiron sites in proteins as well as previous low molecular weight analogues. Crystallographic characterization reveals an anti orientation of the two {Fe(NO)}⁷ (Enemark–Feltham notation) units. The nitrosyl adducts **2** can be (electro)chemically reduced by one electron, as shown by cyclic voltammetry and UV/vis spectroscopy, but without the formation of N₂O. Instead, various spectroscopic techniques including stopped-flow IR spectroscopy indicated the rapid formation, within few seconds, of two well-defined products upon reduction of **2a** (R = Me, X = ClO₄). As shown by IR and Mössbauer spectroscopy as well as X-ray crystallographic characterization, the reduction products are a diiron tetranitrosyl complex ([L{Fe(NO)}₂]₂)(ClO₄), **3a'** and a diacetato-bridged *ferrous* complex [LFe₂(μ-OAc)₂](ClO₄) (**3a''**). Especially **3a'** parallels suggested products in the decay of nitrosylated methane monooxygenase hydroxylase (MMOH), for which N₂O release is much less efficient than for FNORs.



INTRODUCTION

In biological systems, nitric oxide serves several physiological roles, for example, as vasodilator or neurotransmitter.^{1,2} In particular, it is produced by macrophages as a response to invading pathogens, and it thus is an integral part of the immune system.^{3,4} The resulting nitrosative stress should prevent pathogenic bacteria from further proliferation. Several nonheme diiron proteins have been found to exhibit NO detoxification reactivity by conversion of nitric oxide to nitrous oxide (N₂O). In the case of soluble methane monooxygenase hydroxylase (MMOH) and ribonucleotide reductases (RNR), slow conversion rates and low yields of N₂O were observed, whereas flavo-diiron proteins (FDPs) are much better suited for NO reduction.^{5–11} One subclass among the latter, flavo-diiron nitric oxide reductases (FNORs), was found to provide a very efficient pathway of NO scavenging and detoxification.^{5,8,12–16} In a two-electron reduction process these carboxylate-bridged, nonheme diiron centers with a proximal flavin mononucleotide cofactor (FMN) can mediate the conversion of NO to N₂O.¹² As a consequence, the key step in immune defense is abrogated, and the pathogenic bacteria

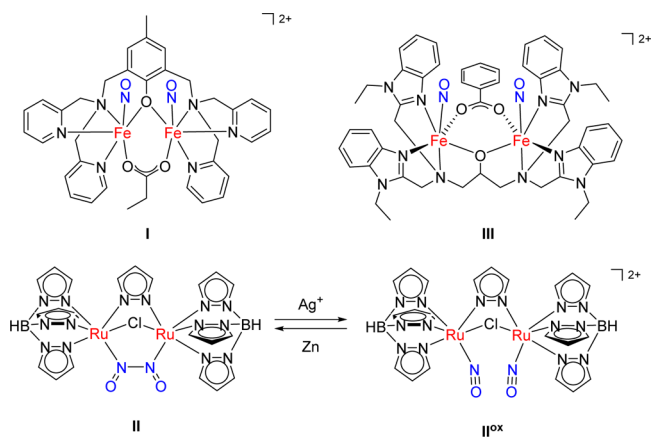
can cause harmful infections. Understanding the mechanism of NO detoxification could provide a valuable starting point for the development of an efficient treatment. However, intermediates and key steps in the reaction catalyzed by FNORs are controversially discussed in literature and have yet to be fully elucidated.^{8,13,15–21}

Basically all current mechanistic proposals involve the formation of a diiron mononitrosyl compound (Fe^{II}{Fe(NO)}⁷ in the Enemark–Feltham²² notation).^{8,19,23} In the hyponitrite mechanism, a second NO molecule directly attacks the {Fe(NO)}⁷ unit to form a hyponitrito ligand. Indeed, this mechanism was supported by Moëne-Loccoz and Siegbahn, based on experimental and computational results.^{24,25} Three other proposals involve binding of a second NO molecule to the second iron center, yielding a diiron dinitrosyl core motif ([{Fe(NO)}⁷]₂). N₂O might then either be produced by spontaneous N–N bond formation (“diferrous-dinitrosyl” mechanism), or it requires an activation of the {Fe(NO)}⁷

Received: August 27, 2016

sites by reduction to potentially highly reactive $\{\text{Fe}(\text{NO})\}^8$ units²⁶ in a “mixed-valent” or “super-reduced” pathway. Multispectroscopic investigations on a flavo-diiron protein by Kurtz and Hendrich however gave clear evidence for the formation of a diiron dinitrosyl complex, therefore ruling out the possibility of the hyponitrite mechanism. They furthermore suggested that N_2O is spontaneously released from the ($\{\text{Fe}(\text{NO})\}^7$)₂ core.^{15,16} In contrast, the alternative scenario of a super-reduced mechanism has received strong support from experimental results obtained by Lehnert and co-workers with the first functional model complex (**I**, Scheme 1),¹⁷ which

Scheme 1. N_2O Producing Dinuclear Iron and Ruthenium Complexes

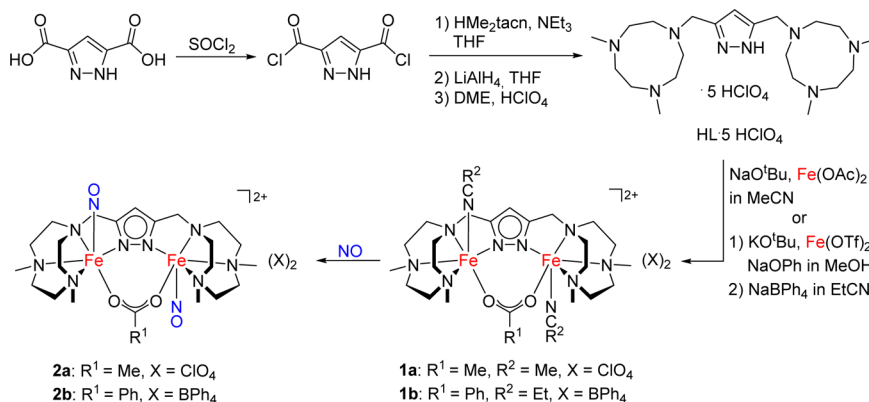


shows quantitative N_2O production from a diiron dinitrosyl complex upon electrochemical or chemical reduction. Theoretical investigations also favor the reduction to $\{\text{Fe}(\text{NO})\}^8$ units prior to N–N bond formation as a key step in N_2O formation in FNORs.¹⁸ The importance of redox events in the transformation of nitrogen oxides was as well highlighted by Arikawa et al., who demonstrated that reversible N–N bond formation in a μ -hyponitrite/nitrosyl-ruthenium analogue (**II** and **II^{ox}**) of an FNOR model complex can be triggered by chemical oxidation or reduction, respectively.²⁷ Furthermore, on the one hand, upon addition of protons, complex **II** was found to release N_2O . On the other hand, Lippard et al. could demonstrate that chemical or electrochemical reduction of a diiron–dinitrosyl complex is not necessarily a prerequisite for N_2O production in model complexes. Using their low

molecular weight analogue **III**, first reported in 1996 and considered as the first structural model for the FNOR active site,²⁸ they recently reported the photochemically induced production of N_2O upon irradiation of **III** at low temperatures (which, however, is likely not biologically relevant).²⁹ Mechanistic details of the reaction are not fully understood and still under investigation.

To gain more insight into possible mechanisms of N_2O formation within the FNOR active site, the development of a broader range of synthetic nonheme diiron analogues is clearly desirable. In this context, we consider several mechanistically relevant factors for NO reduction, namely, (1) an appropriate orientation of the NO binding sites, (2) a suitable $\text{Fe}\cdots\text{Fe}$ distance to allow for N–N bond formation between the nitrosyl ligands, (3) the correct spin state of the bound nitrosyl ligands (as observed in FNORs), (4) redox-activation of the iron-nitrosyl moiety prior to N–N bond formation, and (5) involvement of protons in the overall reduction of NO to N_2O . Studying the redox behavior of diiron (di)nitrosyl complexes and elucidating the factors that may lead to (or prevent) N_2O formation and that may discriminate between different reaction pathways is of particular interest, especially in the light of the discussed mixed-valent or super-reduced mechanism in FNORs. However, few such systems are available, and detailed investigations of their electrochemistry and their reductive transformations are very rare.^{17,23} In this work we introduce a dinucleating pyrazole/triazacyclononane (tacn) hybrid proligand HL as a suitable platform for diiron dinitrosyl chemistry. Similar ligand scaffolds have previously been shown to stabilize metal complexes in different oxidation states and, even more important, their small molecule adducts, which has so far been exploited mainly for metal ions such as zinc, nickel, and copper.^{30–35} We envisioned that the ligand scaffold L^- should provide two pockets for hosting two iron ions in close proximity. Together with an exogenous carboxylate coligand that serves as a secondary bridge within the bimetallic pocket,³⁶ a pentadentate coordination sphere for each metal ion was anticipated, leaving a vacant sixth coordination site for substrate binding, that is, for nitric oxide. In the following, the synthesis of two new *ferrous* diiron compounds with HL is reported, which readily react with nitric oxide to form stable diiron dinitrosyl complexes. The bioinspired reductive transformations of those NO adducts have been comprehensively studied.

Scheme 2. Synthesis of the Ligand Framework and Dinitrosyl Complex Used in This Work



RESULTS AND DISCUSSION

Synthesis of Ligand Precursor and Ferrous Compounds. The synthesis of the new proligand HL used in this work is schematically depicted in Scheme 2; it is based on protocols reported previously for the derivative with peripheral isopropyl substituents^{37,38} and the parent ligand devoid of any N-substituents,^{39,40} with minor modifications. The commercially available synthon 3,5-pyrazole dicarboxylic acid monohydrate was converted into the more reactive acid chloride by treatment with thionyl chloride.⁴¹ Introduction of the macrocyclic side arm and subsequent reduction gave the pyrazole/tacn proligand HL as a highly viscous oil. After protonation with concentrated perchloric acid in 1,2-dimethoxy ethane (DME), it could be isolated in solid form as HL·5HClO₄ in sufficient purity for subsequent complexation studies.

Treatment of HL·5HClO₄ with iron(II) acetate and sodium-*tert*-butoxide in MeCN gave a light orange reaction mixture. After removal of all solid material, slow diffusion of diethyl ether into the solution led to the formation of colorless to light orange crystals of acetate-bridged complex **1a**. The benzoate-bridged derivative was obtained by reacting HL·5HClO₄ with iron(II) perchlorate in the presence of potassium-*tert*-butoxide and sodium benzoate in methanol solution. Addition of sodium tetraphenylborate resulted in the precipitation of a yellow solid, which was redissolved in EtCN. Crystalline material could then be obtained by slow diffusion of diethyl ether into the solution, yielding yellow crystals of compound **1b**. The isolated compounds were sensitive toward moisture and dioxygen and thus had to be handled under strictly anaerobic conditions.

Characterization of **1a and **1b** in Solid State.** Molecular structures of complexes **1a** and **1b** in solid state are shown in Figure 1. In both cases, the overall coordination sphere was found to be very similar. L[−], the carboxylate coligand, and solvent molecules provide a {N₅O} donor set and a roughly octahedral coordination sphere for each iron center. In case of **1b** a crystallographic C₂ axis through the pyrazole and carboxylate units leads to equivalent iron ions; that is, the asymmetric unit contains only one-half of the cation. In both bimetallic molecules, the C₂ axis (noncrystallographic in case of **1a**) reflects an anti orientation of the two nitrile ligands with respect to the central core defined by the pyrazolate plane, the carboxylate, and the two metal ions. In benzoate-bridged **1b** the Fe···Fe distance is slightly larger (4.35 Å) than in acetate-bridged **1a** (4.20 Å), likely due to packing effects that lead to different tilting of the carboxylate bridge as reflected by the Fe–O···O–Fe dihedral angles (32° in **1a** and 11° in **1b**).

⁵⁷Fe Mössbauer experiments, which were performed on crystalline samples of **1a** and **1b** at 80 K, revealed the presence of exclusively high-spin iron(II) sites. The experimental data together with a simulation of the spectra can be found in Figure 2 (top). Isomer shifts of both complexes are very similar, $\delta = 1.11$ and 1.14 mms^{−1} for **1a** and **1b**, respectively. The quadrupole splittings, however, differ substantially ($|\Delta E_Q| = 1.36$ mms^{−1} for **1a** and $|\Delta E_Q| = 2.32$ mms^{−1} for **1b**). A reasonable explanation for this might be the differing Fe–O···O–Fe dihedral angle identified in the solid-state structures, which was shown to have a pronounced influence on the quadrupole splitting in related carboxylate-bridged diiron(II) complexes.⁴² Indeed, measuring zero-field ⁵⁷Fe Mössbauer spectra of **1a** in frozen MeCN solution and **1b** in frozen EtCN solution revealed rather similar quadrupole splitting for both compounds (~1.90 mms^{−1}; see Supporting Information for

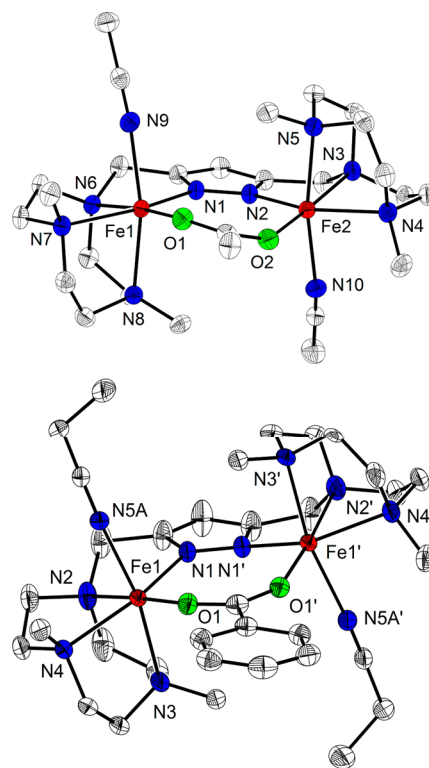


Figure 1. (top) Molecular structure of the cation of **1a** together with a partial labeling scheme; thermal displacement ellipsoids are drawn at 50% probability. Hydrogen atoms and counterions were omitted for clarity. Selected bond lengths [Å] for **1a**: Fe1···Fe2 4.1993(10), Fe2–O2 2.0419(14), Fe1–O1 2.0439(15), Fe2–N2 2.0662(17), Fe1–N1 2.0771(16), Fe2–N4 2.2013(16), Fe1–N7 2.2122(16), Fe2–N10 2.2361(17), Fe1–N9 2.2365(17), Fe2–N5 2.2419(16), Fe1–N8 2.2558(16), Fe1–N6 2.2678(17), Fe2–N3 2.2742(17). (bottom) Molecular structure of the cation of **1b** together with a partial labeling scheme; thermal displacement ellipsoids are drawn at 30% probability. Hydrogen atoms, counterions, and cocrystallized solvent molecules were omitted for clarity. Selected bond lengths [Å] for **1b**: Fe1···Fe1' 4.3512(10), Fe1–O1 2.0417(18), Fe1–N1 2.101(2), Fe1–N5A 2.220(7), Fe1–N3 2.238(2), Fe1–N2 2.251(2), Fe1–N4 2.252(2). Symmetry transformation used to generate equivalent atoms: (') $-x, y, 3/2 - z$.

details). In frozen solution, a distribution of various Fe–O···O–Fe dihedral angles of the carboxylate bridge and varying Fe–N≡C(R) angles can be anticipated. This is also reflected in significantly larger line broadening in the frozen solution spectra (~0.60 mms^{−1} vs ~0.40 mms^{−1} in solid state). Frozen-solution spectra furthermore indicated structural integrity of **1a** and **1b** in nitrile solvents (see Figure S1 and Table S2). The presence of two high-spin iron(II) sites was furthermore confirmed by magnetic measurements, yielding $\chi_m T$ values of 7.33 (**1a**) or 7.40 cm³ K mol^{−1} (**1b**) at 210 K (Figure 2, bottom). Analysis of the data was performed by simultaneously fitting the variable temperature $\chi_m T$ and the variable-temperature variable-field (VTVH) curves (see Figure 2, inset bottom), based on isotropic exchange, zero-field splitting, and Zeeman splitting (see Supporting Information for details). As apparent from the obtained coupling constant of $J \approx 0$ cm^{−1}, exchange coupling via the bridging pyrazole unit and the carboxylate coligand is negligible in both compounds. The sharp decrease of the $\chi_m T$ curve below 50 K in case of **1a** and below 15 K in the case of **1b** was attributed to a sizeable axial zero-field splitting parameter D of ca. −17 cm^{−1} for both

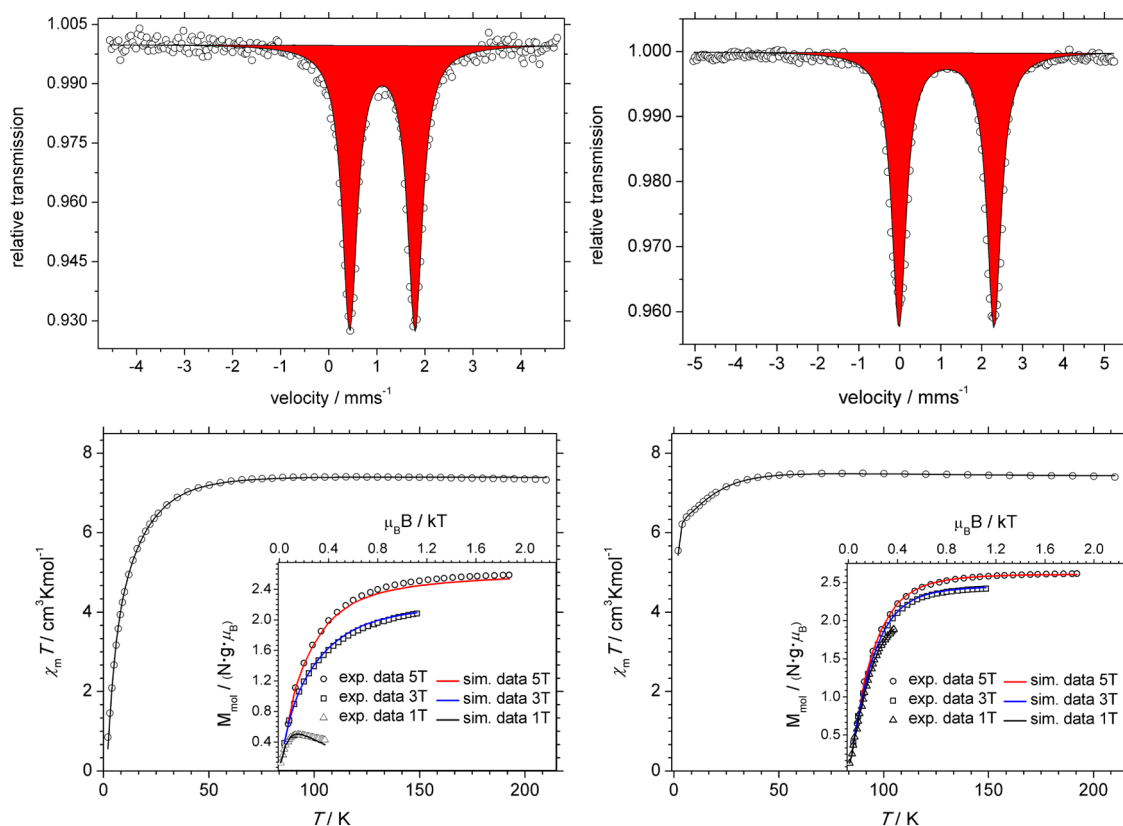


Figure 2. (top) Zero-field Mössbauer spectra of polycrystalline samples of **1a** (left) and **1b** (right), measured at 80 K. (bottom) $\chi_m T$ vs T measurements in the temperature range from 2 to 210 K of **1a** (left) and **1b** (right) at a field of 0.5 T (O: experimental data; solid line: fit). (insets) Variable-temperature/variable-field measurements at fields of 1, 3, and 5 T with the respective fits.

compounds, as confirmed by the VTVH measurements. Here a nesting of the three curves, recorded at 1, 3, and 5 T, was apparent in each measurement. In case of **1b**, rhombicity $E/D = 0.2$ (E is the transverse component of zero-field splitting) was included in the fit. Furthermore, both complexes display very similar anisotropic g values, with principal values of $g_x = g_y = 2.08$, $g_z = 2.45$ for **1a** and $g_x = g_y = 2.10$, $g_z = 2.42$ for **1b**.

Characterization of the Nitrosylation Products. While solutions of **1a** and **1b** are colorless or slightly yellow, exposure toward nitric oxide gas leads to an immediate change in color, giving greenish-brown solutions of **2a** or **2b**. Accordingly, the UV–vis absorbance spectra (which for **1a** and **1b** are essentially featureless above 300 nm) change upon nitrosylation to yield spectra dominated by a band at 445 nm ($\epsilon = 1540 \text{ M}^{-1} \text{ cm}^{-1}$) and two very broad absorptions around 560 ($\epsilon = 325 \text{ m}^{-1} \text{ cm}^{-1}$) and 675 nm ($\epsilon = 240 \text{ m}^{-1} \text{ cm}^{-1}$). These spectroscopic characteristics compare reasonably well with the deflavinated FDP nitrosyl adduct that features absorption maxima at 450 ($\epsilon = 1000 \text{ m}^{-1} \text{ cm}^{-1}$) and 638 nm ($\epsilon \approx 200 \text{ m}^{-1} \text{ cm}^{-1}$), which were assigned to $\text{NO} \rightarrow \text{Fe}$ ligand-to-metal charge transfer and d–d transitions, respectively.^{19,43,44} This gave a first indication that the nitrile ligands in **1a/1b** were substituted by NO upon exposure toward nitric oxide gas. However, the method of choice for following the exchange is IR spectroscopy, since the NO stretch in iron–nitrosyl complexes is usually prominent and can also be probed by isotopic labeling (see below). Indeed, comparison of spectra of starting materials **1a** or **1b** and their nitrosylated analogues (given in Figure 3) revealed that the $\text{C} \equiv \text{N}$ stretches around 2300 cm^{-1} disappear, whereas a very prominent band arises at 1740 cm^{-1} for **2a** and 1745

cm^{-1} for **2b**. These band positions of the NO stretches are in good agreement with those of naturally occurring nonheme dinitrosyl compounds as well as with the IR characteristics of other model systems (see Table 1).

Structural characterization of **2a** and **2b** was hampered by solubility issues, because the nitrosyl complexes proved to be far less soluble than their precursors **1a** and **1b**. This low solubility mostly led to the precipitation of microcrystalline, though analytically pure, powders of the dinitrosyl compounds after diethyl ether or methyl *tert*-butyl ether diffusion into their solutions in nitrile solvents. After careful optimization of the crystallization conditions, single crystals could be obtained for benzoate complex **2b**. It crystallizes in the triclinic space group $P\bar{1}$ with two independent complex molecules as well as one propionitrile molecule in the asymmetric unit. In the following, averaged structural parameters for all four crystallographically distinct $\{\text{Fe}(\text{NO})\}^7$ moieties will be discussed, and only one dication is depicted in Figure 4. In the bimetallic dication of **2b**, the overall coordination geometry of the precursor complex **1b** is preserved, meaning that the complex results from the formal substitution of the nitrile ligands by nitric oxide to form two $\{\text{Fe}(\text{NO})\}^7$ units per dication. The $\text{Fe} \cdots \text{Fe}$ distance remains virtually unchanged (4.33 vs 4.35 \AA in **1b**), and again each iron center is located in an approximately octahedral $\{\text{N}_5\text{O}\}$ coordination sphere. Whereas the $\text{Fe} - \text{N}^{\text{taco}}$ bond lengths range from 2.17 to 2.28 \AA , the distances to donor atoms of the anionic (co)ligands are significantly shorter ($2.01 \pm 0.02 \text{ \AA}$ for $\text{Fe} - \text{O}^{\text{benz}}$ and $2.08 \pm 0.02 \text{ \AA}$ for $\text{Fe} - \text{N}^{\text{Pz}}$). The average $\text{Fe} - \text{NO}$ distance is $(1.77 \pm 0.01) \text{ \AA}$ with an average $\text{N} - \text{O}$ bond length of $(1.15 \pm 0.01) \text{ \AA}$, whereby a decrease in $d(\text{Fe} - \text{NO})$ is

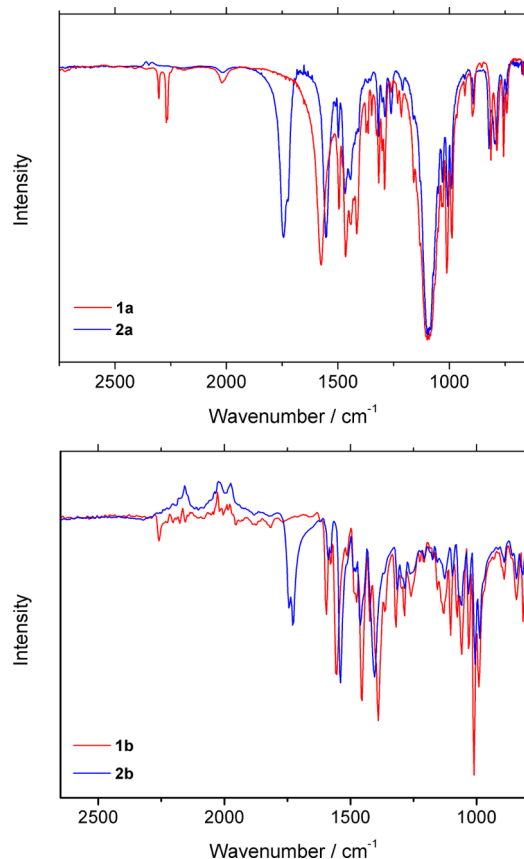


Figure 3. (top) IR spectra of solid nitrile complex **1a** and its nitrosyl analogue **2a** (KBr matrix). (bottom) IR spectra of solid nitrile complex **1b** and its nitrosyl analogue **2b** (KBr matrix).

correlated with an increase in $d(\text{N}-\text{O})$. These rather long Fe–NO distances are in line with the strongly anionic ligand set and compare well with metric parameters of previously reported model systems, as do the N–O bond lengths in **2b**. A detailed comparison of structural parameters of **2b**, **I**, and **III** can be found in Table 1. All Fe–NO units in **2b** are slightly bent with angles Fe–N–O in the range of 149–154°, which is common for $\{\text{Fe}(\text{NO})\}_7$ units featuring a ligand environment free of sterical constraints, because deviation from linearity stabilizes the Fe–NO bond due to backbonding interactions between the $\text{Fe}(d_z^2)$ - and NO-based orbitals.^{45,46}

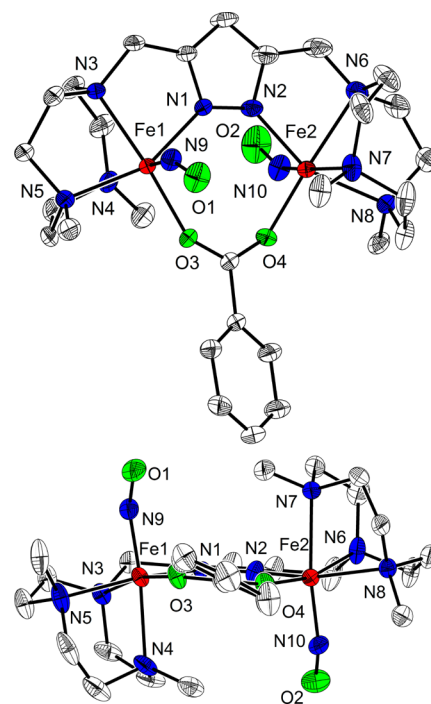


Figure 4. Molecular structure representations (two different views; the lower part shows a frontal view to highlight the anti orientation of the Fe–NO moieties) of one of the crystallographically independent cations of **2b** together with a partial labeling scheme; thermal displacement ellipsoids are given at 50%. Solvent molecules, tetraphenylborate anion, and hydrogen atoms are omitted for clarity. Selected bond lengths [Å] for **2b** (Fe3 and Fe4 refers to the second crystallographically independent cation): Fe1⋯Fe2 4.3422(18), Fe3⋯Fe4 4.3095(14), Fe1–N9 1.758(4), Fe2–N10 1.764(4), Fe3–N19 1.771(4), Fe4–N20 1.778(3), Fe2–O4 1.997(3), Fe1–O3 2.001(3), Fe4–O8 2.020(3), Fe3–O7 2.033(3), Fe2–N2 2.050(3), Fe4–N12 2.060(3), Fe3–N11 2.089(3), Fe1–N1 2.101(4), O1–N9 1.162(5), O2–N10 1.162(5), O5–N19 1.133(5), O6–N20 1.156(4).

Zero-field ^{57}Fe Mössbauer spectra for **2a** and **2b** were measured at 80 K, and in both cases an asymmetric subspectrum was used to fit the overall spectrum (see Figure 5); the asymmetry of the spectra is probably caused by magnetic relaxation effects.⁴⁷ Spectroscopic parameters for both compounds are very similar (**2a**: $\delta = 0.63 \text{ mms}^{-1}/|\Delta E_Q| = 1.38 \text{ mms}^{-1}$; **2b**: $\delta = 0.65 \text{ mms}^{-1}/|\Delta E_Q| = 1.43 \text{ mms}^{-1}$). Since the

Table 1. Comparison of Spectroscopic and Metric Parameters of $\{\{\text{Fe}(\text{NO})\}_7\}_2$ Units in FDP, RNR, sMMO, and Low Molecular Weight Analogues **I**, **III**, and **2b**

	FDP ^{13,16}	RNR ^{10,11}	MMOH ⁹	I ¹⁷	III ²⁸	2b
Fe⋯Fe (Å)				3.47	3.44	4.33 ^a
Fe–N(O) (Å)				1.774	1.749	1.768 ^a
				1.796	1.750	
N–O (Å)				1.157	1.151	1.153 ^a
				1.172	1.156	
Fe–N–O (deg)				156/145	167/168	151 ^a
$\bar{\nu}(\text{N}-\text{O})$ (cm ⁻¹)	1749	1730		1760	1785	1745
δ (mms ⁻¹)	0.71	0.75, 0.75	0.72	n.r.	0.67	0.65
$ \Delta E_Q $ (mms ⁻¹)	1.85	2.13, 1.73	1.55	n.r.	1.44	1.43
λ (nm)						
$[\epsilon$ (M ⁻¹ cm ⁻¹)]	455 [1000], 638 [n.r.] ^b	450 [760], 620 [220] ^b	450 [740], 620 [n.r.]	410 [n.r.]	520 [395], 620 [9579]	445 [1540], 560 [325], 675 [240]

^aAveraged value for all four Fe(NO)₇ units in the asymmetric unit; ^bPer iron; n.r. not reported.

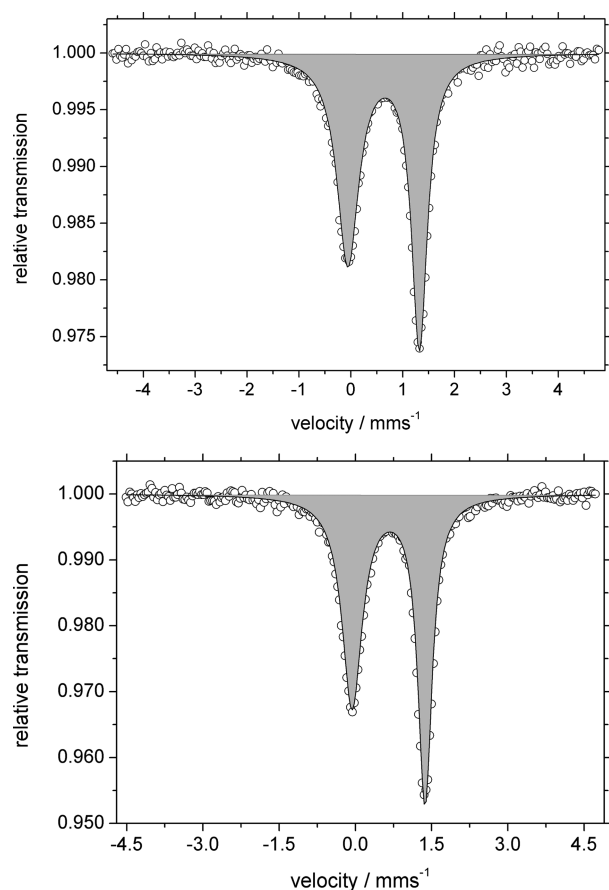


Figure 5. Zero-field Mössbauer spectra of **2a** (top) and **2b** (bottom) recorded for powdered samples; (○) experimental data; the solid black lines represent the overall fit of the spectra, using one asymmetric subspectrum (depicted in light gray).

quadrupole splitting in general is very sensitive toward the coordination environment of the iron centers, close structural similarity between **2a** and **2b** can be assumed (especially for the anti orientation of the NO ligands, which was also observed in the nitrile precursors **1a** and **1b**), even though crystallographic information for **2a** is not available. The data are furthermore consistent with ^{57}Fe Mössbauer parameters of other diiron dinitrosyl sites, namely, the dinitrosyl adducts of FDP,¹⁶ RNR,¹⁰ and MMOH,⁹ as well as **III**²⁸ (see Table 1).

Reduction: Electrochemistry and Spectroscopy. Compounds **2a** and **2b** are stable in solution; they neither undergo spontaneous formation of N_2O nor show a significant loss of NO ligands in solution when kept under N_2 . The pivotal role of electron transfer processes prior to N_2O release in **I** as well as (potentially) in FNOR prompted us to investigate the redox properties of **2a** and **2b** in more detail. For this purpose, cyclic voltammograms were recorded in dichloromethane (DCM) solutions, using $n\text{-Bu}_4\text{NPF}_6$ (0.1M) as conducting salt (see Figure 6 and Supporting Information). Indeed, at a potential of ca. -1.1 V (vs the Fc/Fc^+ couple), an irreversible reduction wave was found for both complexes. In the reverse scan new signals including a reversible redox process at ca. -0.45 V occurred, indicating the formation of chemically distinct species after the initial reduction process. Reduction potentials of **2a** and **2b** are similar to those reported for other $\{\text{Fe}(\text{NO})\}_2^7$ units,^{17,19,23} suggesting that the reduction occurs at the iron-nitrosyl moieties. Two equivalents of CoCp_2 ($E^0 = -1.33$ V vs

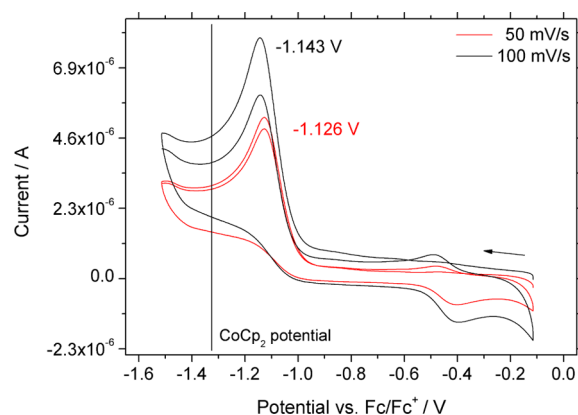


Figure 6. Cyclic voltammogram of **2a** in DCM/0.1 M NBu_4PF_6 at room temperature vs the Fc/Fc^+ couple at scan rates of 50 (solid red line) and 100 mV s^{-1} (solid black line); two consecutive scans are shown for both scan rates; peak potentials of the reductive wave are indicated.

Fc/Fc^+ in DCM)⁴⁸ were added to a solution of **2a** in DCM, but no N_2O gas evolution was detected via headspace analysis upon chemical reduction. Titration of a solution containing **2a** with aliquots of CoCp_2 furthermore revealed that the reduction of compound **2a** is complete upon addition of only 1 equiv of CoCp_2 per diiron dinitrosyl complex cation (see Supporting Information), meaning that on average only one $\{\text{Fe}(\text{NO})\}_2^7$ unit per complex is reduced. This is in contrast to what was observed for **I**, for which the uptake of two electrons was found, followed by the release of N_2O . The lack of nitrous oxide formation in case of **2a** can probably be rationalized by the anti orientation of the NO ligands, preventing intramolecular N–N bond formation and thus leading to a different decomposition pathway of the reduced complex. In fact, for nonheme diiron-dinitrosyl complexes, a syn configuration of the NO units is seen as a prerequisite for intramolecular N_2O formation.¹⁰ As the cyclic voltammograms of **2a** and **2b** indicate an ECE (= electron transfer, chemical reaction, electron transfer) mechanism in which 1e^- reduction is followed by a chemical reaction and the formation of distinct reduction products, their nature was more closely investigated by spectroscopic methods.

To that end, the reduction of a bulk solution of **2a** was performed both electrochemically (Figure 7) and chemically (by addition of stoichiometric amounts of CoCp_2) and monitored by IR spectroscopy; products with the same spectroscopic features were obtained by either of the two reduction methods. Major changes were observed in the $\tilde{\nu}$ (N–O) range as well as for the band arising from the asymmetric carboxylate stretch. The NO absorption of **2a** at 1740 cm^{-1} vanishes upon reduction, while a new band attributed to the NO ligands in the reduced species arises at 1670 cm^{-1} , whereas the carboxylate stretch shifts from 1555 to 1610 cm^{-1} . Band assignment was corroborated by $^{15}\text{N}^{18}\text{O}$ labeling, where only one of the two bands (within the solvent window) was found to be sensitive upon isotope exchange and is thus associated with the N–O vibration. The band at 1740 cm^{-1} for unlabeled **2a** shifts to 1669 cm^{-1} in the $^{15}\text{N}^{18}\text{O}$ complex, which is in agreement with a harmonic oscillator behavior ($\Delta\tilde{\nu}$ (N–O) = -71 cm^{-1}). The NO-sensitive band in the product resulting from the reduction of **2a** displays a much larger apparent isotopic shift of $\Delta\tilde{\nu}$ (N–O) = -121 cm^{-1} , which would by far be too large for a simple harmonic oscillator. We rationalize this with the formation of an $\{\text{Fe}(\text{NO})_2\}_2^x$ unit formed upon

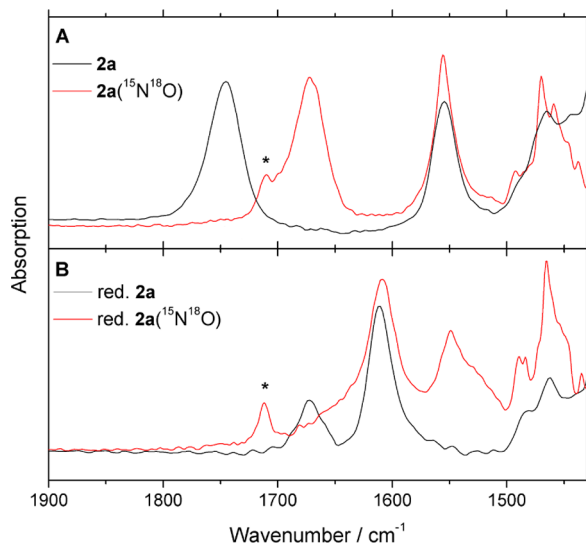


Figure 7. (top) Comparison of IR spectra for **2a** and its isotopologue obtained from a reaction of **1a** with $^{15}\text{N}^{18}\text{O}$ (**2a**($^{15}\text{N}^{18}\text{O}$)). (bottom) Comparison of IR spectra for electrochemically reduced **2a** and electrochemically reduced **2a**($^{15}\text{N}^{18}\text{O}$). The asterisk marks an unidentified impurity that was occasionally observed.

reduction (see below and [Supporting Information](#) for properties of the isolated material and structure determination).⁴⁹ Therefore, we propose that the spectrum contains two signals for NO-based stretches, being typical for $\{\text{Fe}(\text{NO})_2\}^x$ fragments,^{49–51} one at 1670 cm^{-1} and one being obscured by the strong asymmetric carboxylate stretch between 1580 and 1630 cm^{-1} . Upon isotope exchange the 1670 cm^{-1} band shifts to $\sim 1610\text{ cm}^{-1}$ (which is now concealed by the nonshifting carboxylate stretch, [Figures 7](#) and [10](#)), whereas the formerly hidden band shifts to 1549 cm^{-1} and thus becomes visible. As expected, bands assigned to the asymmetric carboxylate stretch of the exogenous coligand are virtually unaffected when using $^{15}\text{N}^{18}\text{O}$ in **2a** as well as in the respective reduction products ($\sim 1610\text{ cm}^{-1}$). Still, **2a** and the reduced mixture exhibit very distinct differences in the asymmetric carboxylate stretch, indicating major changes in the coordination mode of the carboxylate coligands.

To provide further spectroscopic insight into the chemical processes following reduction, frozen-solution Mössbauer spectra were recorded. For this a crystalline sample of **2a** was dissolved in a tetrahydrofuran (THF)/MeCN mixture inside a glovebox and mixed with 1.1 equiv of CoCp_2 . Within some seconds the reaction mixture turned from dark brownish-green to red-brown. The solution was placed in a sample holder and immersed in liquid nitrogen directly after transferring the sample out of the glovebox. Analysis of the ^{57}Fe Mössbauer spectrum revealed that compound **2a** was entirely consumed and that two new distinct iron species were present in the sample ([Figure 8](#)). One of the subspectra, accounting for 57% of the iron content, displayed typical parameters for a *ferrous* high-spin complex with an isomer shift of $\delta = 1.16\text{ mms}^{-1}$ and a quadrupole splitting of $|\Delta E_Q| = 2.66\text{ mms}^{-1}$. A second doublet represented 43% of the total iron sites. On the basis of its isomer shift of $\delta = 0.48\text{ mms}^{-1}$ and the quadrupole splitting of $|\Delta E_Q| = 0.50\text{ mms}^{-1}$, this doublet had to arise from an iron species with more *ferric* character than the previously discussed species, and it was therefore assigned to the $\{\text{Fe}(\text{NO})_2\}^x$ site ($x = 9/10$). Comparison to Mössbauer parameters of literature-

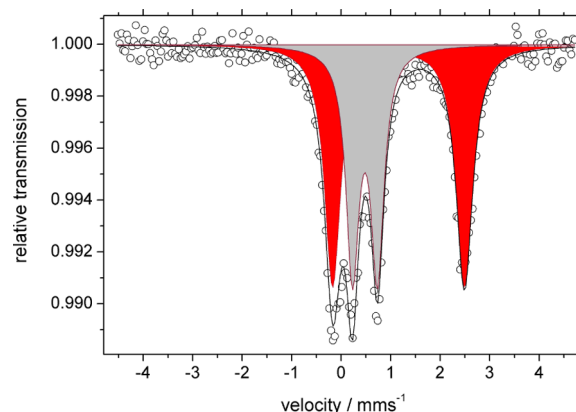


Figure 8. ^{57}Fe Mössbauer spectrum of a frozen THF/MeCN solution of **2a** after reduction with 1.1 equiv of CoCp_2 , recorded at 80 K. The solid black line represents the overall fit of the spectrum, whereas the red and gray areas depict the calculated Lorentzian profiles of two individual subspectra (\circ experimental data).

known complexes did not allow for a conclusive assignment of the redox level in the $\{\text{Fe}(\text{NO})_2\}^x$ unit. Isomers shifts for those complexes are usually found in a wide range between 0.05 and 0.64 mms^{-1} ,^{52–56} being mostly influenced by the nature of the coligands and less by the actual redox level of the $\{\text{Fe}(\text{NO})_2\}^x$ site.^{52,56} Charge balance considerations, though, indicate the formation of an $\{\text{Fe}(\text{NO})_2\}^9$ species, since the uptake of only one redox equivalent per molecule **2a** together with the formation of a *ferrous* species was detected. Combined, the results obtained from IR and Mössbauer spectroscopies suggested a major rearrangement of the ligand sphere around the iron ions, involving the formation of a dinitrosyl iron center, as well as a change in the coordination mode of the carboxylate coligand.

Reduction: Structural Insights. The Mössbauer spectrum with two well-defined subspectra in an almost 1:1 ratio⁵⁷ indicated that the chemical reaction following $1e^-$ reduction of **2a** leads to clean conversion to either a single complex with two distinct iron sites or to two separate reaction products. Subsequently, isolation of the reaction product(s) in crystalline form was attempted for unambiguous identification. To that end, diethyl ether was slowly diffused into reaction mixtures containing CoCp_2 -treated **2a**. Overnight three different types of crystals formed; decoloration of the supernatant liquid indicated precipitation of the reaction products. One of the compounds was dark brown with block-shaped crystals, in the following referred to as **3a'**. Furthermore, the formation of almost colorless needles was observed (**3a''**). A yellow crystalline precipitate was found as a third compound and was identified as $[\text{CoCp}_2]\text{ClO}_4$; the three types of products could partially be separated manually (see [Experimental Section](#)). Crystals of **3a'** and **3a''** proved suitable for X-ray diffraction studies ([Figure 9](#)). The monocationic complex **3a'** crystallizes in the monoclinic space group $P2_1/c$ and has two equivalent iron sites due to crystallographic C_2 symmetry. The cation contains two $\{\text{Fe}(\text{NO})_2\}^9$ fragments hosted by the tacn/pyrazolate ligand framework L^- . The coordination geometry around both iron sites can be described as slightly distorted from octahedral. Because of the missing second bridging ligand, the $\text{Fe}\cdots\text{Fe}$ distance expands to 4.49 \AA . The $\text{Fe}-\text{N}(\text{O})$ distances are 1.74 and 1.76 \AA , with an angle between both $\text{Fe}-\text{NO}$ units of 97.4° ($\text{N5}-\text{Fe}-\text{N6}$). Since the NO ligands are bent toward each other, their orientation resembles the

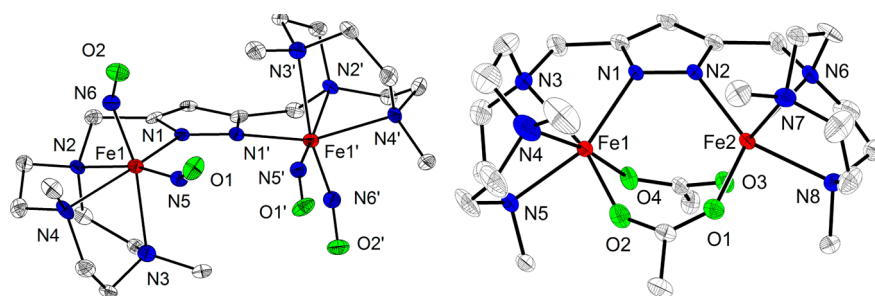


Figure 9. (left) Molecular structure representation of the cationic portion of $3a'$ together with a partial labeling scheme; thermal displacement ellipsoids are given at 30%, hydrogen atoms and the perchlorate counterion are omitted for clarity. Selected bond lengths [\AA] for $3a'$: Fe1...Fe1' 4.486(3), Fe1–N5 1.737(9), Fe1–N6 1.758(11), Fe1–N1 2.104(8), Fe1–N4 2.205(9), Fe1–N2 2.284(9), Fe1–N3 2.357(11). Symmetry transformation used to generate equivalent atoms: (') $1 - x, y, 1/2 - z$. (right) Molecular structure representation of the cationic portion of $3a''$ together with a partial labeling scheme; thermal displacement ellipsoids are given at 30%; the perchlorate anion and hydrogen atoms are omitted for clarity. Selected bond lengths [\AA] for the major disordered part in $3a''$: Fe1...Fe2 3.7732(13), Fe1–O1 2.0487(18), Fe2–O4 2.0702(19), Fe2–N2 2.095(2), Fe2–O2 2.0967(18), Fe1–N1 2.136(3), Fe1–O3 2.1424(17), Fe1–N5 2.173(14), Fe2–N8 2.197(12), Fe2–N7 2.214(12), Fe1–N4 2.248(7), Fe1–N3 2.275(9), Fe2–N6 2.336(7).

“attracto” conformation in tetrahedral complexes. To the best of the authors’ knowledge, such a tetranitrosyl diiron complex supported by a dinucleating N-donor ligand scaffold is unprecedented in the literature. Usually, tetranitrosyl diiron complexes resemble iron–sulfur clusterlike structures, with oxides or sulfides as bridging ligands (Roussin’s red salt or “esters”).^{49,58–62} Interestingly, a compound structurally analogous to $3a'$ has been proposed by Lippard et al. as a minor decay product of the dinitrosyl adduct of MMOH, likewise containing an $\{\text{Fe}(\text{NO})_2\}_2$ core motif. Mössbauer and IR spectra recorded for crystalline material of $3a'$ ($\delta = 0.48 \text{ mms}^{-1}$, $|\Delta E_Q| = 0.49 \text{ mms}^{-1}$, $\sim 10 \text{ mg}$ sample of $3a'$) confirmed that $3a'$ represents one of the two iron-containing components in the reaction mixture resulting from the reduction of $2a$ (see Supporting Information).⁶³ The IR spectrum of isolated $3a'$, measured as a KBr pellet, exhibits a strong band at 1690 cm^{-1} for $\tilde{\nu}(\text{N–O})$, which is slightly shifted in comparison with data for a DCM solution of $3a'$ (1670 cm^{-1}); such differences of NO stretching frequencies for solid and solution samples are not unprecedented.^{26,52} In addition, a rather strong band at 1575 cm^{-1} can be observed (see Figure 10), which is obscured in IR spectra of the mixed reduction products in solution by the

strong asymmetric carboxylate stretch at 1610 cm^{-1} , as discussed above. Both features at 1690 and 1575 cm^{-1} are assigned to N–O vibrations (symmetric and antisymmetric), with a band separation of $\Delta\tilde{\nu}(\text{N–O}) = 115 \text{ cm}^{-1}$ being typical for six-coordinate $\{\text{Fe}(\text{NO})_2\}_2$ moieties.^{49–51}

Structural insight into the second distinct species obtained from chemical reduction of $2a$ revealed a diacetato-bridged diiron(II) complex, supported by L^- . This complex ($3a''$) crystallizes in the triclinic space group $P\bar{1}$; the asymmetric unit contains one complex cation and one perchlorate anion. Both iron sites in the cation are surrounded by a $\{\text{N}_4\text{O}_2\}$ donor set, which forms a rather distorted octahedral environment. Because of the presence of three bridging units (pyrazolate and two exogenous acetate ligands) and the resulting structural constraints, the pyrazolate plane is severely tilted with respect to the Fe1/N1/N2/Fe2 plane. Besides, the Fe...Fe distance (3.77 \AA) is much more contracted in $3a''$ in comparison with $1a$, $1b$, or $2b$. Isolation of a few crystals allowed for the recording of an IR spectrum of pure $3a''$ in a KBr matrix, confirming the presence of a strong band at 1610 cm^{-1} as it was observed for the reaction mixture resulting from the reduction of $2a$ (Figure 10). Analysis of isolated $3a''$ by Mössbauer spectroscopy, though, was hampered by the low yield and contamination of the bulk material with large amounts of cobaltocenium salts as well as with some $3a'$.

Mechanistic Considerations. Having identified the final products of the reduction process according to Scheme 3, mechanistic insight into details of the ligand rearrangements was sought. Because $2a$ as well as both reaction products $3a'$ and $3a''$ exhibit distinct IR bands, the development of all identified species could be followed independently by time-resolved IR spectroscopy. Initial experiments indicated a fast process on the time scale of seconds, so the use of a stopped-flow technique was required. Thus, DCM solutions of $2a$ were rapidly mixed anaerobically with a DCM solution of CoCp_2 under pseudo-first-order conditions (1:10 equiv, $10 \text{ }^\circ\text{C}$), and the development of the IR signatures was monitored for several seconds. Unfortunately, the asymmetric carboxylate stretch of $2a$ was not visible under the experimental conditions (the lower limit of reproducible spectra was $\sim 1575 \text{ cm}^{-1}$). Other spectroscopic marker features for all three species (1765 cm^{-1} for $2a$, 1675 cm^{-1} for $3a'$, and 1605 cm^{-1} for $3a''$) were reproduced reasonably well under stopped-flow conditions. Kinetic traces (Figure 11) reveal that the depletion of the IR

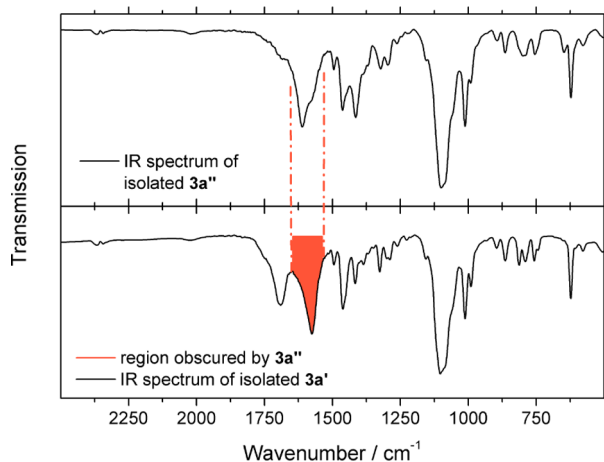


Figure 10. IR spectra of isolated compounds $3a'$ and $3a''$ (KBr matrix). The orange region marks the strong absorption of the asymmetric carboxylate stretch in $3a''$, which conceals the second NO-based stretch in $3a'$.

Scheme 3. Overall Reduction Process of Complex 2a

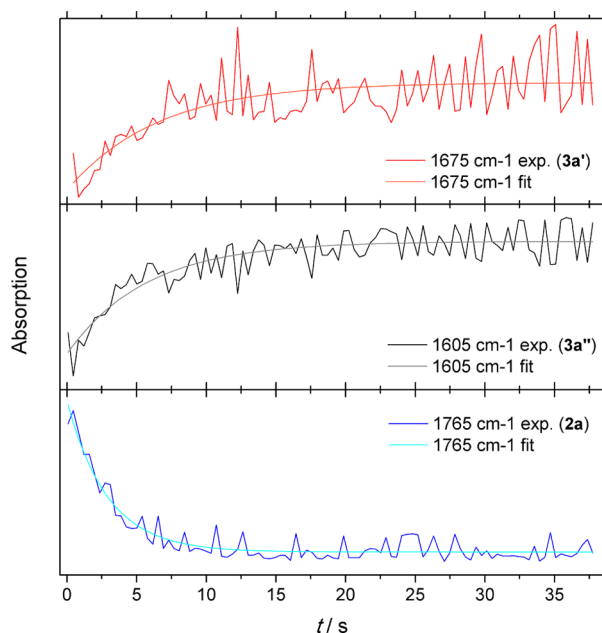
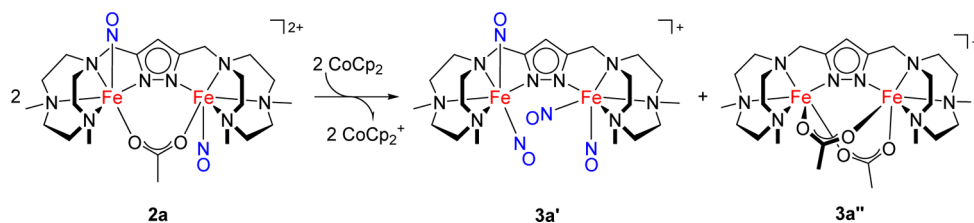


Figure 11. Kinetic traces obtained from stopped-flow IR spectroscopy. (top) Experimental trace and pseudo-first-order fit of the band at 1675 cm^{-1} , characteristic for $3a'$. (middle) Time-resolved development of the band at 1605 cm^{-1} ($3a''$) together with the pseudo-first-order fit. (bottom) Decay of the band at 1765 cm^{-1} ($2a$) and the corresponding pseudo-first-order fit.

band associated with the $\{\text{Fe}(\text{NO})\}^7$ in $2a$ is significantly faster than the rise of both the band of the asymmetric carboxylate stretch in $3a''$ and the band associated with the $\{\text{Fe}(\text{NO})_2\}^9$ units in $3a'$. Averaged over three runs, k_{obs} for the decay of $2a$ is $0.704 \pm 0.169 \text{ s}^{-1}$, whereas for the formation of $3a'$ as well as $3a''$ essentially identical pseudo-first-order rate constants of 0.208 ± 0.08 and $0.225 \pm 0.083 \text{ s}^{-1}$, respectively, were determined. Because of the high signal-to-noise ratio as well as the low resolution of the spectra (8 cm^{-1} to enhance temporal resolution), no features of any potential intermediate, such as an $\{\text{Fe}(\text{NO})\}^8$ unit, could be identified. The differences in rate constants, however, suggest that decay of $2a$ to $3a'$ and $3a''$ is not a concerted reaction. It seems feasible though that reduction triggers the release of NO^- , which causes a cascade of further ligand dissociations and rearrangement processes. Intra- or intermolecular redox events also must play a role in this cascade.

CONCLUSIONS

In this report, we have demonstrated the formation of bioinspired diiron–dinitrosyl adducts supported by a dinucleating pyrazolate/tacn hybrid ligand scaffold L^- and by an exogenous carboxylate bridge. $[\text{L}\{\text{Fe}(\text{NO})\}_2(\mu\text{-OAc})](\text{ClO}_4)_2$ ($2a$) and $[\text{L}\{\text{Fe}(\text{NO})\}_2(\mu\text{-OBz})](\text{BPh}_4)_2$ ($2b$) are readily

formed upon reaction of nitric oxide gas with their analogous precursor complexes $[\text{L}\{\text{Fe}(\text{MeCN})\}_2(\mu\text{-OAc})](\text{ClO}_4)_2$ ($1a$) and $[\text{L}\{\text{Fe}(\text{EtCN})\}_2(\mu\text{-OBz})](\text{BPh}_4)_2$ ($1b$) that have labile nitrile coligands. According to spectroscopic and structural data, $2a$ and $2b$ contain two $\{\text{Fe}(\text{NO})\}^7$ moieties and represent rare examples of diiron–dinitrosyl compounds, which can be regarded as model systems for the active site of FNORs. In contrast to previous low molecular weight analogues, crystallographic analysis revealed an anti orientation of both NO ligands in $2a$. As a consequence, reduction of $2a$ at a potential of -1.1 V leads to transfer of only a single electron and triggers a cascade of subsequent ligand scrambling reactions, instead of $2e^-$ reduction followed by N_2O release as observed for previously reported I ,¹⁷ which featured the two NO ligands in syn positions.

Ligand rearrangement processes following reduction of $2a$ are rapid and within a few seconds lead to the diiron–tetranitrosyl complex $[\text{L}\{\text{Fe}(\text{NO})_2\}_2](\text{ClO}_4)$ ($3a'$) and the bis(acetate)-bridged diferrous complex $[\text{LFe}_2(\mu\text{-OAc})_2](\text{ClO}_4)$ ($3a''$) as final products. Rate constants for the decay of $2a$ and formation of $3a'$ and $3a''$ differ, suggesting a complex stepwise scenario, but intermediate species are too short-lived and could not be detected even by stopped-flow IR spectroscopy. In particular, it remains unclear whether $1e^-$ reduction of $2a$ initially leads to intramolecular ligand rearrangement within the L^- scaffold, giving a mixed-valent species that has a $\{\text{Fe}(\text{NO})_2\}^9$ unit next to a ferrous subsite with the (potentially chelating) acetate, specifically, an $[\text{Fe}(\text{II})\text{-}\{\text{Fe}(\text{NO})_2\}^9]$ intermediate. Alternatively, NO^- may be released to directly initiate diffusion-controlled intermolecular ligand exchange.

Diiron–tetranitrosyl complex $3a'$ appears to be the first structurally characterized $[\{\text{Fe}(\text{NO})_2\}^9]_2$ complex supported by a preorganized dinucleating ligand scaffold. Such an $[\{\text{Fe}(\text{NO})_2\}^9]_2$ species was suspected to partially form in the decay of nitrosylated MMOH, leading to a lower efficiency of this enzyme in $\text{NO}/\text{N}_2\text{O}$ transformation when compared to FNOR active sites.⁹ A low efficiency was also reported for the nitrosylated R2 unit of RNR,¹⁰ which was ascribed to the partial formation of an *anti* $[\{\text{Fe}(\text{NO})\}^7]_2$ form. Our work is in line with these results and highlights the importance of a proper syn configuration with a short $\text{O}\equiv\text{N}\cdots\text{N}\equiv\text{O}$ distance for enabling the N_2O formation process.

EXPERIMENTAL SECTION

Caution! Although no problems were encountered during this work, note that metal perchlorates are potentially explosive and should be handled with care, and they should be prepared only in small quantities. Work with perchloric acid must be conducted with proper precautions.

The syntheses of all air- and moisture-sensitive ligands, building blocks, or complexes were performed under inert atmosphere (dry argon or dinitrogen) using standard Schlenk techniques or in a glovebox. All glassware was dried at $120 \text{ }^\circ\text{C}$ overnight prior to use. Solvents were purified and dried according to established procedures; prior to use they were distilled and degassed by bubbling with argon.

For complex synthesis, the solvents were further degassed using at least three freeze–pump–thaw cycles. Na_2CO_3 was dried at 120°C at 1×10^{-5} mbar for 1 d. $\text{Fe}(\text{OAc})_2$ as well as 2,4-dimethyl-1,4,7-triazacyclononane were synthesized according to literature procedures.^{64,65} All other chemicals were purchased from commercial sources and used without further purification. ^1H and $^{13}\text{C}\{^1\text{H}\}$ NMR spectra were recorded on a Bruker Avance 300 MHz spectrometer; chemical shifts are reported in parts per million relative to residual proton signals of the solvents. Electrospray ionization (ESI) mass spectra were recorded on a Bruker HCT Ultra spectrometer coupled to a glovebox. Microanalyses were performed by the “Analytic Laboratory of the Institute for Inorganic Chemistry at the University of Göttingen”, using a Vario EL III. IR spectra were recorded with a Bruker VERTEX 70 using KBr pellets, solution IR cells with KBr or CaF_2 windows, or IR gas cells with KBr windows, operated with the OPUS program. UV/vis spectra were measured with a Cary 5000 Bio spectro-photometer using quartz cuvettes sealed with a rubber septum.

X-ray data were collected on an STOE IPDS II diffractometer with an area detector (graphite monochromated $\text{Mo K}\alpha$ radiation, $\lambda = 0.71073 \text{ \AA}$) by use of ω scans at 133 K (for details see Table S1). The structures were solved using direct methods and refined against F^2 using all reflections with SHELX-2013.⁶⁶ Face-indexed absorption corrections were performed by the program X-RED.⁶⁷ For details concerning the structure refinement see Supporting Information.

Mössbauer spectra were recorded with a ^{57}Co source in a Rh matrix using an alternating constant WissEl Mössbauer spectrometer, consisting of an MR 360 Drive Unit, an MV-1000 velocity transducer, and an LND 45431 proportional counter mounted on an LINOS precision bench. The system was operated in a horizontal transmission geometry with source, absorber, and detector in a linear arrangement. The temperature was controlled and maintained using a Janis SHI closed-cycle helium cryostat. Data acquisition was performed using a 512 channel analyzer. Isomer shifts were referenced versus α -iron metal foil at ambient temperatures. Simulation of experimental data was performed using the *Mfit* program⁶⁸ (see Supporting Information for a detailed description of the fits). Temperature-dependent magnetic susceptibilities were measured using a Quantum-Design MPMS XL-5 SQUID magnetometer equipped with a 5 T magnet. The polycrystalline sample was contained in a gelatin capsule, fixed with polyfluorinated oil if necessary, and placed in a nonmagnetic sample holder. Each raw data file for the magnetic moment was corrected for the diamagnetic contribution of the gelatin capsule according to $M^{\text{dia}}(\text{capsule}) = \chi g \times m \times H$, with an experimentally obtained gram susceptibility of the gelatin capsule. The molar susceptibility data were corrected for the diamagnetic contribution using the Pascal constants and the increment method according to Haberditzl.^{69,70} Magnetic properties were simulated with the *julX* program⁷¹ (for a detailed description of the fitting procedures and fitted parameters see Supporting Information).

Cyclic voltammetry was performed with an EG&G272 A potentiostat or a CH instruments CHI600E workstation. Cyclic voltammograms were recorded by using a three-electrode arrangement with a glassy carbon working electrode (2 mm diameter), a Ag wire reference electrode, and a Pt wire counter electrode. Ferrocene was added as an internal standard after the measurements. All potentials were referenced relative to the Fc/Fc^+ couple. For bulk electrolysis followed by IR spectroscopy, the respective solution was placed in a solution IR cell with CaF_2 windows. Electrodes consist of an 8×10 mm Pt mesh (100 mesh, 99.9%, Aldrich) for the working electrode, 3×10 mm Pt mesh for the counter electrode, and an Ag wire (0.1 mm, 99.9%) as a reference electrode. For IR measurements a PerkinElmer BX or a Bruker VERTEX 70 spectrometer was used. The IR stopped-flow measurements were performed using a stopped-flow assembly consisting of a TgK Scientific SF-61 syringe drive operated by the KinetaDrive software. Spectra were monitored using a VERTEX 70 FT-IR spectrometer with a liquid nitrogen cooled MCT detector and a mirror velocity of 160 kHz at a resolution of 8 cm^{-1} in Rapid Scan mode (OPUS software). The path length of the cell was $100 \mu\text{m}$. The samples were prepared inside a glovebox, loaded into Terumo syringes. Together with a second syringe, containing blank, degassed

solvent, it was connected to a three-way valve (chrome plated brass, Luer Lock) and transferred out of the glovebox. The blank solvent was used to rinse all tubings and the sample cell and to record background spectra before loading the stopped-flow device with **2a** or CoCp_2 . Because of a high signal-to-noise ratio, the obtained spectra were usually smoothed in the data processing part.

Synthesis of $\text{HL}\cdot 5\text{HClO}_4$. Under vigorous stirring neat thionyl chloride (120 mL) was added to 3,5-pyrazole dicarboxylic acid monohydrate (600 mg, 3.45 mmol). The suspension was heated to 90°C for 15 h. Subsequently all volatile material was removed under reduced pressure. The remaining white solid was taken up in THF (75 mL), and a solution of 2,4-dimethyl-1,4,7-triazacyclononane (1.16 g, 7.38 mmol) and NEt_3 (1.5 mL) in THF (25 mL) was added dropwise. The green suspension was stirred overnight at room temperature, filtered, and evaporated to complete dryness. The remaining solid was dissolved in THF (20 mL) and added dropwise to a suspension of LiAlH_4 (310 mg, 37.9 mmol) in THF (50 mL). The resulting suspension was refluxed for 10 h. After it cooled to room temperature, the reaction was quenched by the careful addition of water, filtered, and evaporated to dryness. Light petroleum (40 mL) was added, and the mixture was heated to reflux until the residue dissolved no further (~ 24 h). The light petroleum fraction was then evaporated, and the colorless oil was taken up in DME (4 mL). Precipitation with concentrated hydroperchloric acid (70% by weight), washing with $\text{EtOH}/\text{Et}_2\text{O}$ (1:5), and drying in vacuo gave the product $\text{HL}\cdot 5\text{HClO}_4$, as determined by NMR with NaOBz as internal standard, as an off-white solid (1.3 g, 1.44 mmol, 42%). ^1H NMR (300 MHz, CD_3CN): δ (ppm) = 3.10 (s, 12 H, CH_3), 3.30–3.39 (m, 8 H CH_2), 3.43–3.50 (m, 8 H, CH_2), 3.71 (s, 8 H, CH_2), 4.05 (s, 4 H, CH_2), 6.46 (s, 1 H, CH^{pz}). $^{13}\text{C}\{^1\text{H}\}$ NMR (75 MHz, CD_3CN): δ (ppm) = 18.7 (CH_3), 48.4 (CH_2), 52.4 (CH_2), 57.9 (CH_2), 58.8 (CH_2), 72.3 (4-C^{pz}). $3\text{-C}^{\text{pz}}/5\text{-C}^{\text{pz}}$ were not observed in the spectrum.

Synthesis of $[\text{L}\{\text{Fe}(\text{MeCN})_2(\mu\text{-OAc})\}(\text{ClO}_4)_2$ (1a**).** $\text{HL}\cdot 5\text{HClO}_4$ (100 mg, 100 μmol) and NaO^tBu (53 mg, 0.55 mmol) were suspended in MeCN (3 mL), and the mixture was stirred for 5 to 10 min. This was followed by the addition of iron(II) acetate (38 mg, 219 μmol). Stirring was continued for 4 h, and then the suspension was filtered. The light yellow solution was placed in a crystallization vessel. Slow diffusion of Et_2O gave light yellow crystals of the desired complex **1a** (70 mg, 82 μmol , 75%). IR (KBr): $\tilde{\nu}/\text{cm}^{-1} = 757 \text{ m}, 787 \text{ m}, 814 \text{ m}, 896 \text{ w}, 988 \text{ m}, 1011 \text{ s}, 1034 \text{ m}, 1095 \text{ s}, 1215 \text{ w}, 1291 \text{ m}, 1317 \text{ m}, 1365 \text{ w}, 1415 \text{ m}, 1466 \text{ s}, 1494 \text{ m}, 1577 \text{ s}, 2270 \text{ w}, 2304 \text{ w}, 2897 \text{ m}$. Elemental analysis calcd. (%) for $\text{C}_{27}\text{H}_{50}\text{Cl}_2\text{Fe}_2\text{N}_{10}\text{O}_{10}$ (found): 37.82 (37.69), 5.88 (6.09), 16.34 (16.25).

Synthesis of $[\text{L}\{\text{Fe}(\text{MeCN})_2(\mu\text{-OBz})\}(\text{BPh}_4)_2$ (1b**).** $\text{HL}\cdot 5\text{HClO}_4$ (100 mg, 110 μmol) and KO^tBu (80 mg, 0.64 mmol) were suspended in MeOH (5 mL). NaOBz (19 mg, 132 μmol) was added to the resulting suspension, and stirring continued for 5 min. $\text{Fe}(\text{ClO}_4)_2 \cdot 10 \text{H}_2\text{O}$ (100 mg, 230 μmol), dissolved in MeOH (1 mL), was added dropwise. Stirring the suspension overnight led to a color change from green to yellow-brown. Solid material was filtered off, and the clear solution was treated with NaBPh_4 (76 mg, 222 μmol) in MeOH (1 mL). The yellow precipitate was isolated by decantation of the supernatant liquid and redissolved in EtCN. Slow diffusion of Et_2O into the solution gave the desired complex **1b** as yellow crystals (58 mg, 42 μmol , 38%). IR (KBr): $\tilde{\nu}/\text{cm}^{-1} = 430 \text{ w}, 468 \text{ w}, 574 \text{ w}, 613 \text{ s}, 624 \text{ m}, 666 \text{ m}, 707 \text{ s}, 735 \text{ s}, 748 \text{ s}, 789 \text{ w}, 816 \text{ m}, 841 \text{ w}, 891 \text{ w}, 991 \text{ w}, 1012 \text{ m}, 1032 \text{ m}, 1066 \text{ m}, 1078 \text{ m}, 1103 \text{ m}, 1261 \text{ m}, 1288 \text{ m}, 1321 \text{ m}, 1393 \text{ s}, 1424 \text{ m}, 1455 \text{ s}, 1476 \text{ m}, 1487 \text{ m}, 1558 \text{ m}, 1579 \text{ m}, 2260 \text{ m}, 2872 \text{ m}, 2922 \text{ m}, 2996, 3053 \text{ m}$. Elemental analysis calcd. (%) for $\text{C}_{82}\text{H}_{96}\text{B}_2\text{Fe}_2\text{N}_{10}\text{O}_2$ (found): 71.01 (70.74), 6.98 (7.11), 10.10 (9.97).

Synthesis of $[\text{L}\{\text{Fe}(\text{NO})_2(\mu\text{-OAc})\}(\text{ClO}_4)_2$ (2a**).** Compound **1a** (44.6 mg, 52.0 μmol) was dissolved in EtCN (2 mL) and transferred into a crystallization vessel filled with methyl tertiary butyl ether (MTBE). The headspace of the vessel was then shortly evacuated and refilled with nitric oxide gas. After 2 d, the desired NO compound was obtained as a green-brown solid. The supernatant liquid was subsequently removed by syringe, and the microcrystalline material shortly dried under vacuum (30.2 mg, 36.3 μmol , 70%). The vessel was transferred into a glovebox; the solid material was isolated and

stored at $-36\text{ }^{\circ}\text{C}$. MS (ESI(+), MeCN): $m/z = 288.2$ $[\text{M} - 2\text{NO}]^{2+}$. IR (KBr): $\tilde{\nu}/\text{cm}^{-1} = 673$ w, 745 w, 759 w, 796 m, 823 m, 892 m, 992 s, 1007 s, 1032 s, 1049 s, 1097 vs, 1210 w, 1261 m, 1289 m, 1319 m, 1443 m, 1467 m, 1498 m, 1553 s, 1740 s, 2865 m, 2966 m. UV/vis (MeCN): $\lambda_{\text{max}}/\text{nm}$ ($\epsilon/(\text{L mol}^{-1} \text{cm}^{-1})$) = 445 (1540), 560 (330), 675 (250). Elemental analysis calcd. (%) for $\text{C}_{23}\text{H}_{44}\text{Cl}_2\text{Fe}_2\text{N}_{10}\text{O}_{12}$ (found): 33.07 (33.03), 5.31 (5.36), 16.77 (16.65).

Synthesis of $[\text{L}\{\text{Fe}(\text{NO})_2\}(\mu\text{-OBz})](\text{BPh}_4)_2$ (2b). Compound 1b (35.8 mg, 25.3 mmol) was dissolved in EtCN (2.5 mL) and transferred into a crystallization vessel filled with MTBE. The headspace of the vessel was shortly evacuated, and the pressure then equilibrated with nitric oxide gas. The desired NO compound was obtained after 2 d as a green-brown solid. Remaining supernatant liquid was taken off by syringe, and the solid shortly dried under vacuum (33.3 mg, 24.4 μmol , 96%). The vessel was transferred into a glovebox, the solid material was isolated, and the crystals were stored at $-36\text{ }^{\circ}\text{C}$. Crystals suitable for X-ray diffraction studies were also obtained by slow diffusion of MTBE into less concentrated EtCN solutions (~ 15 mg in 2 mL), also using smaller test tubes in the crystallization vessel (~ 0.7 mm in diameter). MS (ESI(+), MeCN): $m/z = 319.2$ $[\text{M} - 2\text{NO}]^{2+}$. IR (KBr): $\tilde{\nu}/\text{cm}^{-1} = 441$ m, 484 w, 581 m, 610 s, 663 m, 703 vs, 750 m, 790 w, 815 w, 840 w, 894 w, 988 m, 1006 m, 1030 w, 1059 w, 1095 w, 1124 w, 1207 w, 1282 w, 1313 w, 1407 s, 1459 m, 1478 w, 1579 w, 1599 s, 1726 s, 1746 s, 2870 w, 2924 w, 2995 w, 3035 w. UV/vis (MeCN): $\lambda_{\text{max}}/\text{nm}$ ($\epsilon/(\text{L mol}^{-1} \text{cm}^{-1})$) = 445 (1540), 560 (325), 675 (240). Elemental analysis calcd. (%) for $\text{C}_{76}\text{H}_{86}\text{B}_2\text{Fe}_2\text{N}_{10}\text{O}_4$ (found): 68.28 (67.18), 6.53 (6.49), 10.47 (10.77).

Synthesis of $[\text{L}\{\text{Fe}(\text{NO})_2\}](\text{ClO}_4)$ (3a') and $[\text{LFe}_2(\mu\text{-OAC})_2](\text{ClO}_4)$ (3a''). A typical procedure for the synthesis of 3a' and 3a'' was performed as follows: cobaltocene (5.2 mg, 27 μmol) was dissolved in THF (0.4 mL) and added to a suspension of 2a (19.5 mg, 23.4 μmol) in THF/MeCN (1:1, 0.5 mL). The resulting dark brown solution was stirred for 5 min and placed in crystallization vessel. Over the course of 2 d, diethyl ether was allowed to diffuse into the mixture, whereupon dark brown and yellow as well as almost colorless crystals formed. The three kinds of crystals were sorted manually and analyzed separately. The yellow material represents $[\text{CoCp}_2](\text{ClO}_4)$. Per run ~ 6 –8 mg of 3a' (dark brown blocks) of sufficient purity could be isolated, which were used to record the Mössbauer spectrum depicted in Figure S3 (isolated material of two runs partially combined). Similar attempts to isolate 3a'' to record a Mössbauer spectrum did not yield enough crystalline material of 3a''. Note, though, that the colorless needles of 3a'' were always contaminated with crystallites of 3a' and $[\text{CoCp}_2](\text{ClO}_4)$, and separation of larger amounts of 3a'' from the other products proved to be impossible (needles did not withstand manual separation). Approximately 2 mg of rather clean 3a'' could be isolated per run, which was used for IR analysis; the formed amount of 3a'' based on visual inspection of the crystallized material, though, was much higher. 3a': IR (KBr): $\tilde{\nu}/\text{cm}^{-1} = 463$ m, 505 w, 578 w, 621 s, 741 w, 758 m, 792 m, 818 m, 863 m, 895 w, 988 m, 1014 vs, 1160 w, 1224 w, 1258 w, 1288 m, 1297 m, 1322 m, 1382 m, 1416 m, 1459 s, 1493 m, 1553 m, 1690 s, 2817 w, 2860 m, 2920 m, 2968 w, 3001 w, 3115 m. 3a'': IR (KBr): $\tilde{\nu}/\text{cm}^{-1} = 581$ w, 623 m, 650 w, 756 w, 791 w, 801 w, 865 w, 991 m, 1012 s, 1098 vs, 1156 w, 1261 w, 1300 w, 1324 w, 1416 m, 1465 m, 1497 w, 1611 s, 2820 w, 2893 w, 2921 w, 2970 w, 2997 w.

■ ASSOCIATED CONTENT

● Supporting Information

The Supporting Information is available free of charge on the ACS Publications website at DOI: 10.1021/acs.inorgchem.6b02080.

Crystallographic details of all structurally characterized compounds; Mössbauer spectra including details of the fitting procedure and alternative fits; magnetic data including VTVH measurements and details of the fits; UV/vis titration data; IR spectra of the reduction process

and the reduction products, including time-resolved experiments. (PDF)

X-ray crystallographic information. (CIF)

■ AUTHOR INFORMATION

Corresponding Author

*E-mail: franc.meyer@chemie.uni-goettingen.de.

Notes

The authors declare no competing financial interest.

■ ACKNOWLEDGMENTS

Financial support from the Fonds der Chemischen Industrie, the Studienstiftung des deutschen Volkes (fellowships to N.K.), and the DFG (International Research Training Group IRTG 1422 "Metal Sites in Biomolecules: Structures, Regulation and Mechanisms") is gratefully acknowledged. Short-term research stays of N.K. and A.S. at the Univ. of Michigan, Ann Arbor, were supported by a travel grant of the Georg-August-University (Göttingen International). N.L. acknowledges support from the National Science Foundation for this work (CHE-1305777).

■ REFERENCES

- (1) Balligand, J.-L.; Kelly, R. A.; Marsden, P. A.; Smith, T. W.; Michel, T. Control of cardiac muscle cell function by an endogenous nitric oxide signaling system. *Proc. Natl. Acad. Sci. U. S. A.* **1993**, *90*, 347–351.
- (2) Snyder, S. H. Nitric oxide: first in a new class of neurotransmitters? *Science* **1992**, *257*, 494–496.
- (3) MacMicking, J.; Xie, Q.-W.; Nathan, C. Nitric Oxide and Macrophage Function. *Annu. Rev. Immunol.* **1997**, *15*, 323–350.
- (4) Bogdan, C. Nitric oxide and the immune response. *Nat. Immunol.* **2001**, *2*, 907–916.
- (5) Kurtz, D. M., Jr. Flavo-diiron enzymes: nitric oxide or dioxygen reductases? *Dalton Trans.* **2007**, 4115–4121.
- (6) Romão, C. V.; Vicente, J. B.; Borges, P. T.; Frazão, C.; Teixeira, M. The dual function of flavodiiron proteins: oxygen and/or nitric oxide reductases. *JBIC, J. Biol. Inorg. Chem.* **2016**, *21*, 39–52.
- (7) Frederick, R. E.; Caranto, J. D.; Masitas, C. A.; Gebhardt, L. L.; MacGowan, C. E.; Limberger, R. J.; Kurtz, D. M. Dioxygen and nitric oxide scavenging by *Treponema denticola* flavodiiron protein: a mechanistic paradigm for catalysis. *JBIC, J. Biol. Inorg. Chem.* **2015**, *20*, 603–613.
- (8) Khatua, S.; Majumdar, A. Flavodiiron nitric oxide reductases: Recent developments in the mechanistic study and model chemistry for the catalytic reduction of NO. *J. Inorg. Biochem.* **2015**, *142*, 145–153.
- (9) Coufal, D. E.; Tavares, P.; Pereira, A. S.; Hyunh, B. H.; Lippard, S. J. Reactions of Nitric Oxide with the Reduced Non-Heme Diiron Center of the Soluble Methane Monooxygenase Hydroxylase. *Biochemistry* **1999**, *38*, 4504–4513.
- (10) Haskin, C. J.; Ravi, N.; Lynch, J. B.; Münck, E.; Que, L. Reaction of NO with the Reduced R2 Protein of Ribonucleotide Reductase from *Escherichia coli*. *Biochemistry* **1995**, *34*, 11090–11098.
- (11) Lu, S.; Libby, E.; Saleh, L.; Xing, G.; Bollinger, J. M.; Moënne-Loccoz, P. Characterization of NO adducts of the diiron center in protein R2 of *Escherichia coli* ribonucleotide reductase and site-directed variants; implications for the O_2 activation mechanism. *JBIC, J. Biol. Inorg. Chem.* **2004**, *9*, 818–827.
- (12) Silaghi-Dumitrescu, R.; Kurtz, D. M., Jr.; Ljungdahl, L. G.; Lanzilotta, W. N. X-ray Crystal Structures of Moorella thermoacetica FprA. Novel Diiron Site Structure and Mechanistic Insights into a Scavenging Nitric Oxide Reductase. *Biochemistry* **2005**, *44*, 6492–6501.
- (13) Hayashi, T.; Caranto, J. D.; Wampler, D. A.; Kurtz, D. M.; Moënne-Loccoz, P. Insights into the Nitric Oxide Reductase

Mechanism of Flavodiiron Proteins from a Flavin-Free Enzyme. *Biochemistry* **2010**, *49*, 7040–7049.

(14) Missall, T. A.; Lodge, J. K.; McEwen, J. E. Mechanisms of Resistance to Oxidative and Nitrosative Stress: Implications for Fungal Survival in Mammalian Hosts. *Eukaryotic Cell* **2004**, *3*, 835–846.

(15) Caranto, J. D.; Weitz, A.; Giri, N.; Hendrich, M. P.; Kurtz, D. M. A Diferrous-Dinitrosyl Intermediate in the N₂O Generating Pathway of a Deffluinated Flavo-Diiron Protein. *Biochemistry* **2014**, *53*, 5631–5637.

(16) Caranto, J. D.; Weitz, A.; Hendrich, M. P.; Kurtz, D. M. The Nitric Oxide Reductase Mechanism of a Flavo-Diiron Protein: Identification of Active-Site Intermediates and Products. *J. Am. Chem. Soc.* **2014**, *136*, 7981–7992.

(17) Zheng, S.; Berto, T. C.; Dahl, E. W.; Hoffman, M. B.; Speelman, A. L.; Lehnert, N. The Functional Model Complex [Fe₂(BPMP)-(OPr)(NO)₂](BPh₄)₂ Provides Insight into the Mechanism of Flavodiiron NO Reductases. *J. Am. Chem. Soc.* **2013**, *135*, 4902–4905.

(18) Attia, A. A. A.; Silaghi-Dumitrescu, R. Super-Reduced Mechanism of Nitric Oxide Reduction in Flavo-Diiron NO Reductases. *Eur. J. Inorg. Chem.* **2014**, *2014*, 6061–6065.

(19) Berto, T. C.; Speelman, A. L.; Zheng, S.; Lehnert, N. Mono- and dinuclear non-heme iron-nitrosyl complexes: Models for key intermediates in bacterial nitric oxide reductases. *Coord. Chem. Rev.* **2013**, *257*, 244–259.

(20) Hayashi, T.; Caranto, J. D.; Matsumura, H.; Kurtz, D. M.; Moëne-Loccoz, P. Vibrational Analysis of Mononitrosyl Complexes in Hemerythrin and Flavodiiron Proteins: Relevance to Detoxifying NO Reductase. *J. Am. Chem. Soc.* **2012**, *134*, 6878–6884.

(21) Speelman, A. L.; Lehnert, N. Heme versus Non-Heme Iron-Nitroxyl {FeN(H)O}⁸ Complexes: Electronic Structure and Biologically Relevant Reactivity. *Acc. Chem. Res.* **2014**, *47*, 1106–1116.

(22) Enemark, J. H.; Feltham, R. D. Principles of Structure, Bonding, and Reactivity for Metal Nitrosyl Complexes. *Coord. Chem. Rev.* **1974**, *13*, 339–406.

(23) Majumdar, A.; Lippard, S. J. Non-Heme Mononitrosyldiiron Complexes: Importance of Iron Oxidation State in Controlling the Nature of the Nitrosylated Products. *Inorg. Chem.* **2013**, *52*, 13292–13294.

(24) Hayashi, T.; Caranto, J. D.; Matsumura, H.; Kurtz, D. M.; Moëne-Loccoz, P. Vibrational analysis of mononitrosyl complexes in hemerythrin and flavodiiron proteins: Relevance to detoxifying NO reductase. *J. Am. Chem. Soc.* **2012**, *134*, 6878–6884.

(25) Blomberg, L. M.; Blomberg, M. R.; Siegbahn, P. E. Theoretical study of the reduction of nitric oxide in an A-type flavoprotein. *J. Biol. Inorg. Chem.* **2006**, *12*, 79–89.

(26) Speelman, A. L.; Lehnert, N. Characterization of a High-Spin Non-Heme {FeNO}⁸ Complex: Implications for the Reactivity of Iron Nitroxyl Species in Biology. *Angew. Chem., Int. Ed.* **2013**, *52*, 12283–12287.

(27) Arikawa, Y.; Asayama, T.; Moriguchi, Y.; Agari, S.; Onishi, M. Reversible N-N Coupling of NO Ligands on Dinuclear Ruthenium Complexes and Subsequent N₂O Evolution: Relevance to Nitric Oxide Reductase. *J. Am. Chem. Soc.* **2007**, *129*, 14160–14161.

(28) Feig, A. L.; Bautista, M. T.; Lippard, S. J. A Carboxylate-Bridged Non-Heme Diiron Dinitrosyl Complex. *Inorg. Chem.* **1996**, *35*, 6892–6898.

(29) Jiang, Y.; Hayashi, T.; Matsumura, H.; Do, L. H.; Majumdar, A.; Lippard, S. J.; Moëne-Loccoz, P. Light-Induced N₂O Production from a Non-heme Iron-Nitrosyl Dimer. *J. Am. Chem. Soc.* **2014**, *136*, 12524–12527.

(30) Kindermann, N.; Dechert, S.; Demeshko, S.; Meyer, F. Proton-Induced, Reversible Interconversion of a μ -1,2-Peroxo and a μ -1,1-Hydroperoxo Dicopper(II) Complex. *J. Am. Chem. Soc.* **2015**, *137*, 8002–8005.

(31) Kindermann, N.; Bill, E.; Dechert, S.; Demeshko, S.; Reijerse, E. J.; Meyer, F. A Ferromagnetically Coupled (S = 1) Peroxodicopper(II) Complex. *Angew. Chem., Int. Ed.* **2015**, *54*, 1738–1743.

(32) Dalle, K. E.; Gruene, T.; Dechert, S.; Demeshko, S.; Meyer, F. A weakly coupled biologically relevant Cu^{II}(μ - η^1 : η^1 -O₂) *cis*-peroxo adduct. *J. Am. Chem. Soc.* **2014**, *136*, 7428–7434.

(33) Buchler, S.; Meyer, F.; Kaifer, E.; Pritzkow, H. Tunable TACN/pyrazolate hybrid ligands as dinucleating scaffolds for metallobiosite modeling - dinickel(II) complexes relevant to the urease active site. *Inorg. Chim. Acta* **2002**, *337*, 371–386.

(34) Bauer-Siebenlist, B.; Meyer, F.; Farkas, E.; Vidovic, D.; Cuesta-Seijo, J. A.; Herbst-Irmer, R.; Pritzkow, H. Correlation of Structure and Function in Oligonuclear Zinc(II) Model Phosphatases. *Inorg. Chem.* **2004**, *43*, 4189–4202.

(35) Dalle, K. E.; Meyer, F. Modelling Binuclear Metallobiosites: Insights from Pyrazole-Supported Biomimetic and Bioinspired Complexes. *Eur. J. Inorg. Chem.* **2015**, *2015*, 3391–3405.

(36) Burger, B.; Dechert, S.; Große, C.; Demeshko, S.; Meyer, F. Visualising the carboxylate shift at a bioinspired diiron(II) site in the solid state. *Chem. Commun.* **2011**, *47*, 10428–10430.

(37) Dalle, K. E.; Dechert, S.; Meyer, F. Improved Synthesis and Detailed Characterization of a Hybrid Pyrazole-TACN Dinucleating Ligand. *Z. Anorg. Allg. Chem.* **2015**, *641*, 2181–2189.

(38) Meyer, F.; Beyreuther, S.; Heinze, K.; Zsolnai, L. Dinuclear Cobalt(II) Complexes of Pyrazole Ligands with Chelating Side Arms. *Chem. Ber.* **1997**, *130*, 605–613.

(39) Weller, H.; Siegfried, L.; Neuburger, M.; Zehnder, M.; Kaden, T. A. Synthesis and Structures of Dinuclear Metal Complexes of Bis-macrocycles Having a Pyrazole Bridging Unit. *Helv. Chim. Acta* **1997**, *80*, 2315–2328.

(40) Behle, L.; Neuburger, M.; Zehnder, M.; Kaden, T. A. Mono- and Binuclear Copper(II) Complexes of a Bridging Bis[1,4,7-triazacyclononane]. *Helv. Chim. Acta* **1995**, *78*, 693–702.

(41) Acerete, C.; Bueno, M.; Campayo, L.; Navarro, P.; Rodriguez-Franco, M. I.; et al. Formation of Mono- and Di- Nuclear Complexes of Zn²⁺ from a 26 Membered Tetraester Crown of 3,5-Disubstituted Pyrazole Able to Act as Neutral and Dianionic Ligand. *Tetrahedron* **1994**, *50*, 4765–4774.

(42) Burger, B.; Demeshko, S.; Bill, E.; Dechert, S.; Meyer, F. The Carboxylate Twist: Hysteretic Bistability of a High-Spin Diiron(II) Complex Identified by Mössbauer Spectroscopy. *Angew. Chem., Int. Ed.* **2012**, *51*, 10045–10049.

(43) Jackson, T. A.; Yikilmaz, E.; Miller, A. F.; Brunold, T. C. Spectroscopic and computational study of a non-heme iron {Fe-NO}⁷ system: Exploring the geometric and electronic structures of the nitrosyl adduct of iron superoxide dismutase. *J. Am. Chem. Soc.* **2003**, *125*, 8348–8363.

(44) Diebold, A. R.; Brown-Marshall, C. D.; Neidig, M. L.; Brownlee, J. M.; Moran, G. R.; Solomon, E. I. Activation of α -keto acid-dependent dioxygenases: application of an {FeNO}⁷/⁸{FeO₂}⁸ methodology for characterizing the initial steps of O₂ activation. *J. Am. Chem. Soc.* **2011**, *133*, 18148–18160.

(45) Berto, T.; Hoffman, M.; Murata, Y.; Landenberger, K. B.; Alp, E. E.; Zhao, J.; Lehnert, N. Structural and Electronic Characterization of Non-Heme Fe(II)–Nitrosyls as Biomimetic Models of the Fe_B Center of Bacterial Nitric Oxide Reductase. *J. Am. Chem. Soc.* **2011**, *133*, 16714–16717.

(46) Conradie, J.; Quarless, D. A.; Hsu, H.-F.; Harrop, T. C.; Lippard, S. J.; Koch, S. A.; Ghosh, A. Electronic Structure and FeNO Conformation of Nonheme Iron-Thiolate-NO Complexes: An Experimental and DFT Study. *J. Am. Chem. Soc.* **2007**, *129*, 10446–10456.

(47) Gütllich, P.; Bill, E.; Trautwein, A. X. *Mössbauer Spectroscopy and Transition Metal Chemistry - Fundamentals and Applications*; Springer-Verlag: Heidelberg, Germany, 2011.

(48) Connelly, N. G.; Geiger, W. E. Chemical Redox Agents for Organometallic Chemistry. *Chem. Rev.* **1996**, *96*, 877–910.

(49) Tsai, M.-L.; Tsou, C.-C.; Liaw, W.-F. Dinitrosyl Iron Complexes (DNICs): From Biomimetic Synthesis and Spectroscopic Characterization toward Unveiling the Biological and Catalytic Roles of DNICs. *Acc. Chem. Res.* **2015**, *48*, 1184–1193.

- (50) Shih, W.-C.; Lu, T.-T.; Yang, L.-B.; Tsai, F.-T.; Chiang, M.-H.; Lee, J.-F.; Chiang, Y.-W.; Liaw, W.-F. New members of a class of dinitrosyliron complexes (DNICs): the characteristic EPR signal of the six-coordinate and five-coordinate $\{\text{Fe}(\text{NO})_2\}^9$ DNICs. *J. Inorg. Biochem.* **2012**, *113*, 83–93.
- (51) Tsai, F.-T.; Lee, Y.-C.; Chiang, M.-H.; Liaw, W.-F. Nitrate-to-Nitrite-to-Nitric Oxide Conversion Modulated by Nitrate-Containing $\{\text{Fe}(\text{NO})_2\}^9$ Dinitrosyl Iron Complex (DNIC). *Inorg. Chem.* **2013**, *52*, 464–473.
- (52) Speelman, A. L.; Zhang, B.; Silakov, A.; Skodje, K. M.; Alp, E. E.; Zhao, J.; Hu, M. Y.; Kim, E.; Krebs, C.; Lehnert, N. Unusual Synthetic Pathway for an $\{\text{Fe}(\text{NO})_2\}^9$ Dinitrosyl Iron Complex (DNIC) and Insight into DNIC Electronic Structure via Nuclear Resonance Vibrational Spectroscopy. *Inorg. Chem.* **2016**, *55*, 5485–5501.
- (53) Tonzetich, Z. J.; Do, L. H.; Lippard, S. J. Dinitrosyl Iron Complexes Relevant to Rieske Cluster Nitrosylation. *J. Am. Chem. Soc.* **2009**, *131*, 7964–7965.
- (54) Hess, J. L.; Hsieh, C.; Brothers, S. M.; Hall, M. B.; Darenbourg, M. Y. Self-Assembly of Dinitrosyl Iron Units into Imidazolate-Edge-Bridged Mössbauer Molecular Squares: Characterization Including Mössbauer Spectroscopy. *J. Am. Chem. Soc.* **2011**, *133*, 20426–20434.
- (55) Miki, E.; Motonaga, M.; Mizumachi, K.; Ishimori, T.; Katada, M. Nitrosyliron Complexes Containing 8-Quinolinolate or Its Derivatives. *Bull. Chem. Soc. Jpn.* **1982**, *55*, 2858–2862.
- (56) Pulukkody, R.; Darenbourg, M. Y. Synthetic Advances Inspired by the Bioactive Dinitrosyl Iron Unit. *Acc. Chem. Res.* **2015**, *48*, 2049–2058.
- (57) Deviations from the expected 1:1 ratio may result from different Lamb Mössbauer factors for the two complexes.
- (58) Lee, C.-M.; Chen, C.-H.; Chen, H.-W.; Hsu, J.-L.; Lee, G.-H.; Liaw, W.-F. Nitrosylated Iron-Thiolate-Sulfinate Complexes with $\{\text{Fe}(\text{NO})\}^{6/7}$ Electronic Cores: Relevance to the Transformation between the Active and Inactive NO-Bound Forms of Iron-Containing Nitrile Hydratases. *Inorg. Chem.* **2005**, *44*, 6670–6679.
- (59) Lee, C.-M.; Hsieh, C.-H.; Dutta, A.; Lee, G.-H.; Liaw, W.-F. Oxygen Binding to Sulfur in Nitrosylated Iron-Thiolate Complexes: Relevance to the Fe-Containing Nitrile Hydratases. *J. Am. Chem. Soc.* **2003**, *125*, 11492–11493.
- (60) Lo, F.-C.; Li, Y.-W.; Hsu, I.-J.; Chen, C.-H.; Liaw, W.-F. Insight into the Reactivity and Electronic Structure of Dinuclear Dinitrosyl Iron Complexes. *Inorg. Chem.* **2014**, *53*, 10881–10892.
- (61) Tonzetich, Z. J.; Héroguel, F.; Do, L. H.; Lippard, S. J. Chemistry of Nitrosyliron Complexes Supported by a β -Diketimate Ligand. *Inorg. Chem.* **2011**, *50*, 1570–1579.
- (62) Li, L.; Li, L. Recent advances in multinuclear metal nitrosyl complexes. *Coord. Chem. Rev.* **2016**, *306*, 678–700.
- (63) To ensure homogeneity of the sample, the cell dimensions of several crystals were determined.
- (64) Weber, B.; Betz, R.; Bauer, W.; Schlamp, S. Crystal Structure of Iron(II) Acetate. *Z. Anorg. Allg. Chem.* **2011**, *637*, 102–107.
- (65) Flassbeck, C.; Wieghardt, K. Synthese von N-phenolat-funktionalisierten Makrocyclen des 1, 4, 7-Triazacyclononans sowie des 1-Oxa-4,7-diazacyclononans und ihre Komplexchemie mit Eisen(III). *Z. Anorg. Allg. Chem.* **1992**, *608*, 60–68.
- (66) Sheldrick, G. M. A short history of SHELX. *Acta Crystallogr., Sect. A: Found. Crystallogr.* **2008**, *64*, 112–122.
- (67) STOE & CIE GmbH. X-RED; STOE & CIE GmbH: Darmstadt, Germany, 2002.
- (68) Bill, E. *Mfit*; Max-Planck Institute for Chemical Energy Conversion: Mülheim/Ruhr, Germany, 2008.
- (69) Haberditzl, W. Advances in Molecular Diamagnetism. *Angew. Chem., Int. Ed. Engl.* **1966**, *5*, 288–298.
- (70) Bain, G. A.; Berry, J. F. Diamagnetic Corrections and Pascal's Constants. *J. Chem. Educ.* **2008**, *85*, 532–536.
- (71) Bill, E. *julX*; Max-Planck Institute for Chemical Energy Conversion: Mülheim/Ruhr, Germany, 2008.